IV International Conference on Particle-based Methods – Fundamentals and Applications
PARTICLES 2015
E. Oñate, M. Bischoff, D.R.J. Owen, P. Wriggers & T. Zohdi (Eds)

TWO-PHASE MODELING OF CONDUCTION MODE LASER WELDING USING SMOOTHED PARTICLE HYDRODYNAMICS

Haoyue Hu and Peter Eberhard

Institute of Engineering and Computational Mechanics, University of Stuttgart,
Pfaffenwaldring 9, 70569 Stuttgart, Germany
[haoyue.hu, peter.eberhard]@itm.uni-stuttgart.de
www.itm.uni-stuttgart.de

Key words: SPH, Conduction Mode Laser Welding, Heat Transfer, Phase Transition, Marangoni Convection, Melt Flow

Abstract. The process of conduction mode laser welding is simulated using the meshless Lagrangian method Smoothed Particle Hydrodynamics. The modeling of the solid phase is based on the governing equations in thermoelasticity. For the liquid phase, surface tension effects including the Marangoni force caused by a temperature-dependent surface tension gradient are taken into account to simulate the melt flow in the weld pool. A non-isothermal solid-liquid phase transition with the release or absorption of additional energy known as the latent heat of fusion is considered. The major heat transfer process through conduction is modeled, whereas heat convection and radiation are neglected. The energy input from the laser beam is approximated as a Gaussian heat source acting on the material surface. Numerical results obtained with the developed model are presented for laser spot welding and seam welding of aluminum. The change of process parameters like welding speed and laser power, and their effects on the weld pool dimensions can be investigated through simulations, and the overall welding quality may be assessed.

1 INTRODUCTION

Laser welding is widely applied in industry due to several advantages compared to conventional arc or gas welding: high welding speed, a small heat affected zone, ease of automation, and weight savings. Depending on the absorbed radiation intensity from the laser beam, laser welding may be classified into conduction mode welding and deep penetration welding. Conduction mode laser welding is a preferred manufacturing method to obtain visually appealing weld seams without further grinding or finishing. It is suitable for joining thin sheets and tubes, e.g. visible surfaces of device housings or stainless steel sinks. The process is characterized by high quality welds without defects like pores or spatter, and low mechanical and thermal distortions in the work piece. During the welding

process, a laser beam melts the parts to be welded along a common joint, while the maximum temperature stays below evaporation temperature. The energy is transferred to the work piece merely through heat conduction and thus, the weld depth is limited by the heat conductivity of the material. The molten materials coalesce and solidify to form a weld, whose width is greater than its depth.

To gain insight into the influence of process parameters on the melt flow and resulting weld, the conduction mode laser welding process is simulated using Smoothed Particle Hydrodynamics (SPH) [8, 15]. As a meshless Lagrangian method, it has the ability to accurately describe the free surface melt flow by fulfilling the continuity equation at the same time. The underlying heat transfer phenomena including the solid-liquid interface and the occurring phase transitions, melting and solidification, are modeled based on the works of Cleary and Monaghan [3, 20]. Temperature-dependent material properties are taken into account, as an example, the temperature-dependent surface tension gradient is considered in order to describe the Marangoni convection which dominates the weld pool [11, 24]. The energy input from the laser beam is approximated as a moving heat source acting on the material surface.

2 MODELING WITH SPH

In SPH [16, 18], the continuum is represented by a set of particles acting as discretization points. Material properties and field variables like velocity and acceleration are associated to each particle such that the overall state of the system is characterized properly. The particles interact with each other within a defined influence range h of a smoothing kernel function W. The evaluation of field variables f_i and their derivatives for particle a is approximated by sums over all neighboring particles b

$$f_i^a = \sum_b \frac{m_b}{\rho_b} f_i^b \, W(\mathbf{r}_a - \mathbf{r}_b, h) = \sum_b \frac{m_b}{\rho_b} f_i^b \, W_{ab} \, , \tag{1}$$

$$\frac{\partial f_i^a}{\partial x_j} = -\sum_b \frac{m_b}{\rho_b} f_i^b \, \frac{\partial W(\mathbf{r}_a - \mathbf{r}_b, h)}{\partial x_j} = -\sum_b \frac{m_b}{\rho_b} f_i^b \, \frac{\partial W_{ab}}{\partial x_j} \, , \tag{2}$$

where m is the mass, ρ the density, $\mathbf{r}$ the position vector, and h the smoothing length. The Gaussian kernel function as introduced in [8] is applied here. As a general discretization method, all systems that are described by partial differential equations can be simplified to a set of ordinary differential equations. For time integration, the explicit second-order Leapfrog scheme [21] with time step control is used.

2.1 Solid phase

A coupled thermoelastic approach is developed for modeling the solid phase, in order to analyze both the temperature distribution and the stress and strain in the workpiece during the welding process.

Equation of motion

The balance equation of linear momentum is given as

$$\dot{v}_i = \frac{1}{\rho}\frac{\partial \sigma_{ij}}{\partial x_j} + g_i \tag{3}$$

with the gravity force per unit mass g_i acting as body force. Discretizing this equation into SPH form, the acceleration acting on a particle a due to interaction with its surrounding neighbor particles b is according to [18]

$$\dot{v}_i^{\,a} = \sum_b m_b \left(\frac{\sigma_{ij}^{\,a}}{\rho_a^2} + \frac{\sigma_{ij}^{\,b}}{\rho_b^2} + R_{ij}^{ab}\,\Phi_{ab}^n + \Pi_{ab}\,\delta_{ij} \right) \frac{\partial W_{ab}}{\partial x_j^{\,a}} + g_i \ . \tag{4}$$

For numerical reasons, an artificial stress term $R_{ij}^{ab}\,\Phi_{ab}^n$ introduced in [17] and an artificial viscosity term $\Pi_{ab}\,\delta_{ij}$ proposed in [19, 16] are added in Eq. (4) to reduce the tensile instability and to smooth spurious numerical oscillations, respectively.

The stress tensor consisting of elastic and thermal stresses due to linear thermal expansion is defined as

$$\sigma_{ij} = (-p - 3K\alpha(T - T_0))\delta_{ij} + S_{ij} \ , \tag{5}$$

where p is the pressure, K the bulk modulus, α the thermal expansion coefficient, T the absolute temperature in K, T_0 the reference temperature, and S_{ij} the deviatoric stress tensor. Both the pressure and the thermal expansion term only have influence on the hydrostatic part of the stress tensor.

The hydrostatic part of the stress tensor can be evaluated directly. The pressure is calculated using a state equation. Here, an isothermal approach is chosen

$$p = c_0^2(\rho - \rho_0) \ , \tag{6}$$

where $c_0 = \sqrt{K/\rho_0}$ is the speed of sound, ρ the current density, and ρ_0 the initial reference density.

The Updated Lagrangian method is used for updating the deviatoric part of the stress tensor, which evolves as follows according to [18]

$$\dot{S}_{ij} = 2\mu \left(\dot{\epsilon}_{ij} - \frac{1}{3}\delta_{ij}\dot{\epsilon}_{kk} \right) + S_{ik}\Omega_{jk} + \Omega_{ik}S_{kj} \ , \tag{7}$$

where $\dot{\epsilon}_{ij} = \frac{1}{2}\left(\frac{\partial v_i}{\partial x_j} + \frac{\partial v_j}{\partial x_i}\right)$ is the strain rate tensor, $\Omega_{ij} = \frac{1}{2}\left(\frac{\partial v_i}{\partial x_j} - \frac{\partial v_j}{\partial x_i}\right)$ the rotation rate tensor, and μ the shear modulus. Note that the Jaumann stress rate is employed to ensure the objectivity of the formulation [5].

Energy equation

The thermoelastic coupled heat equation may be derived using the internal energy equation [6]

$$\rho\dot{e} = \sigma_{ij}\dot{\epsilon}_{ij} - \frac{\partial q_i}{\partial x_i} + q_\mathrm{s}\,\delta(\mathbf{r}-\mathbf{R}_\mathrm{s})\;, \tag{8}$$

where e is the specific internal energy, q_i the heat flux, q_s the source strength in the dimension power per unit volume, δ the Dirac delta function, and $\mathbf{R}_\mathrm{s}$ the position vector of the heat source. Inserting the formula for the internal energy density [6]

$$e = c(T-T_0) + \frac{3K}{\rho_0}\alpha T_0\epsilon_{kk} + \frac{1}{2\rho_0}(\lambda+2\mu)\epsilon_{kk}^2 + \frac{\mu}{\rho_0}((\epsilon_{kk})^2+\epsilon_{kk}^2) + \text{const.} \tag{9}$$

with the heat capacity c, the Lamé parameters λ and μ, the approximation $\rho=\rho_0$, and Fourier's law of heat conduction for a material with constant thermal conductivity k

$$q_i = -k\frac{\partial T}{\partial x_i} \tag{10}$$

into Eq. (8) yields the coupled heat equation in linear thermoelasticity

$$\rho c\dot{T} = -3K\alpha T\dot{\epsilon}_{kk} + k\Delta T + q_\mathrm{s}\,\delta(\mathbf{r}-\mathbf{R}_\mathrm{s})\;. \tag{11}$$

Equation (11) is converted to its corresponding SPH form following [3] and [20] for the heat conduction and source term

$$c\dot{T}_a = \sum_b \frac{m_b}{\rho_a\rho_b}\left(-3K\alpha T_a(\mathbf{v}_b-\mathbf{v}_a)\cdot\nabla W_{ab} + 2k(T_a-T_b)F_{ab}\right) + \frac{1}{\rho_a}\sum_k Q_\mathrm{s}\,\zeta_\mathrm{s}W(\mathbf{r}_k-\mathbf{R}_\mathrm{s})\;, \tag{12}$$

where $F_{ab} = (\mathbf{r}_a-\mathbf{r}_b)\cdot\nabla W_{ab}/\|\mathbf{r}_a-\mathbf{r}_b\|^2$, Q_s is the power of the heat source, and ζ_s a normalizing factor for the heat source such that the rate of change of thermal energy is correctly considered [20].

2.2 Liquid phase

The molten material is modeled as an incompressible Newtonian fluid with constant dynamic viscosity η. The constitutive law is characterized following [9] by

$$\sigma_{ij} = -p\delta_{ij} + \eta\left(\frac{\partial v_i}{\partial x_j} + \frac{\partial v_j}{\partial x_i}\right) = -p\delta_{ij} + 2\eta\dot{\epsilon}_{ij}\;, \tag{13}$$

where the pressure is calculated through a quasi-incompressible state equation as given in [1]

$$p = \frac{\rho_0 c_0^2}{\gamma}\left(\left(\frac{\rho}{\rho_0}\right)^\gamma - 1\right) \tag{14}$$

with a constant value $\gamma=7$ and an artificial speed of sound c_0.

Continuity equation

The conservation of mass is ensured by the continuity equation, see [9],

$$\dot{\rho} = -\rho \frac{\partial v_i}{\partial x_i} \tag{15}$$

which is discretized in SPH form as

$$\dot{\rho}_a = \sum_b m_b \frac{\rho_a}{\rho_b} \left(\mathbf{v}_a - \mathbf{v}_b\right) \cdot \nabla W_{ab} \, . \tag{16}$$

Momentum equation

The conservation of linear momentum is described by the Navier-Stokes equation as stated in [9]

$$\rho \dot{v}_i = -\frac{\partial p}{\partial x_i} + \eta \Delta v_i + \rho f_i + \rho g_i \, . \tag{17}$$

The discretization of the pressure term is treated analogously to the pressure term for solid particles in Eq. (4). The viscous forces are modeled by the term proposed in [22]. Additionally, the surface tension force f_i is applied to fluid particles in the melt flow. The computation of the surface tension force is based on the Continuum Surface Force (CSF) model described in [2]. For modeling the Marangoni convection in the melt flow caused by a temperature-dependent surface tension coefficient, we follow the approach from [25]. A linear dependence of the surface tension coefficient τ on temperature with the proportionality factor τ_T is assumed and the volumetric surface tension force is

$$\mathbf{f} = \frac{1}{\rho} \left(\tau \kappa \mathbf{n} + \tau_\mathrm{T} \nabla_\mathrm{s} T\right) , \tag{18}$$

where κ is the curvature, $\mathbf{n}$ the normal vector pointing outwards, and $\nabla_\mathrm{s} T$ the surface temperature gradient. As suggested in [25], $\nabla_\mathrm{s} T$ is projected onto the tangential space and the spatial temperature gradient is calculated using the Corrective Smoothed Particle Method (CSPM) described in [12].

Internal energy equation

The internal energy equation is given in [9] as

$$\rho \dot{e} = \rho c \dot{T} = \frac{\partial v_i}{\partial x_j} \eta \dot{\epsilon}_{ij} + k \Delta T + q_\mathrm{s} \, \delta(\mathbf{r} - \mathbf{R}_\mathrm{s}) \, . \tag{19}$$

Compared to Eq. (11), the coupled term has vanished as a result of incompressibility. Instead, there is a positive viscous dissipation term which represents the energy dissipated as heat.

2.3 Solid-liquid phase transition and interaction

The solid-liquid phase transition is assumed to take place between a significant temperature range, which is the usual case for metal alloys. Therefore, two parameters are set for the phase transition temperature marking the lower solid and upper liquid limit, T_s and T_l. As different material parameters apply for the solid and liquid phase, the temperature dependency is partially considered by using different heat capacities c_s and c_l. During the phase transition from solid to liquid, heat is absorbed by the material. If the absorbed heat value exceeds the latent heat of fusion H_f, the transition has completed. The particle type is then changed from a solid to a fluid particle.

Using the enthalpy method for a non-isothermal phase transition as basis [10], the temperature of each particle is determined from the specific enthalpy h

$$T = \begin{cases} \frac{h}{c_s} & \text{solid: } T < T_s \ , \ h < c_s T_s \ , \\ \left(h + \frac{H_f}{T_l - T_s} T_s\right) \left(c_{in} + \frac{H_f}{T_l - T_s}\right)^{-1} & \text{mushy: } T_s \leq T \leq T_l \ , \ c_s T_s \leq h \leq c_{in} T_l + H_f \ , \\ \frac{1}{c_l}(h - H_f - c_{in}(T_l - T_s)) & \text{liquid: } T \geq T_l \ , \ h \geq c_l T_l + H_f + c_{in}(T_l - T_s) \ . \end{cases} \tag{20}$$

For a continuous function at $T = T_l$, the intermediate heat capacity c_{in} has to fulfill the constraint

$$c_l T_l + H_f + c_{in}(T_l - T_s) = c_{in} T_l + H_f \ , \tag{21}$$

leading to $c_{in} = c_l T_l / T_s$.

The elastic interaction for solid particles given in Eq. (4) is also applied to the interaction between solid and fluid particles. The difference lies in the evaluation of the stress tensor of the fluid particle from Eq. (13). In contrast to other contact algorithms for fluid-structure interaction with SPH that introduce repulsive forces between two approaching particles similar to the penalty contact force scheme [14], or e.g. the CD-FSIT algorithm [13], this approach is purely based on the stress tensors for the solid and fluid particle. The interaction does not contain any additional artificial parameters and hence avoids the cumbersome process of parameter identification. Concerning the energy equation, both Eq. (8) and Eq. (19) are combined. The coupled thermoelastic term is only applied to the solid particle, whereas the viscous dissipation term is solely applied to the fluid particle.

2.4 Laser beam

According to the Beer-Lambert law [24], the laser beam intensity I decreases exponentially with respect to the depth z after penetrating the surface of the workpiece

$$I(z) = (1 - \Gamma) I_0 \exp(-Az) \ , \tag{22}$$

where Γ is the reflection coefficient, and $A = 4\pi n\kappa / \lambda_0$ the absorption coefficient, with the refractivity n, the absorbance κ, and the wave length of the laser beam in vacuum λ_0.

For metals, the depth of absorbing 95 % of the laser radiation is less than one micrometer [11, 24], therefore the laser beam may be regarded as a surface source.

The assumption of a Gaussian intensity distribution is most common when modeling a laser beam. Due to the use of the Gaussian kernel in the presented SPH simulations, the Gaussian intensity distribution is implicitly considered. The power intensity is defined as

$$I(x,y) = \frac{(1-\Gamma)P_{\text{laser}}}{\exp(-0.5)\,\pi r_{\text{s}}^2} \exp\left(-\frac{x^2}{r_{\text{s}}^2} - \frac{y^2}{r_{\text{s}}^2}\right), \tag{23}$$

in which the radius of influence of the heat source r_s is set equal to the smoothing length. Hence, the strength of the heat source is identified as $Q_{\text{s}} = (1-\Gamma)P_{\text{laser}}/\exp(-0.5)$ such that the intensity at the distance $r_{\text{s}}/\sqrt{2}$ is equal to the mean absorbed radiation intensity $(1-\Gamma)P_{\text{laser}}/\pi r_s^2$.

3 SIMULATION RESULTS

For the simulations, the suggested model is implemented into the object-oriented software package Pasimodo [7, 23]. Two exemplary welding processes of aluminum are presented. First, a spot weld generated by a short-term laser heating process and subsequent solidification is modeled. The second example shows a seam welding process with a moving laser beam. As boundary condition, a few bottom layers of particles are fixed in all directions to prevent rigid body motion.

The explicit time integration scheme has to fulfill the Courant-Friedrichs-Lewy condition [4] for the maximum time step to achieve stable results. The limiting factor for the time step is the speed of sound of the material. To reduce the computation time, the speed of sound may be decreased, if the analysis of thermal effects is in the focus and the error in the coupling term of Eq. (11) may be neglected.

3.1 Static heat source

First, we simulate the process of laser spot welding where a static laser beam irradiates the workpiece for 15 ms. The initial temperature distribution is homogeneous at 293 K, no additional temperature boundary conditions are set. The temperature distribution after the heating process is shown in Figure 1. The effect of the Gaussian distribution of the laser radiation on the resulting temperature field is clearly visible.

The Marangoni force acting in the melt flow due to a temperature-dependent surface tension coefficient is plotted in Figure 2. The molten material flows in the negative direction of the temperature gradient and the Marangoni force in x and y-direction have their maxima near the solid-liquid interface. In z-direction, the force is negative with no distinct minimum value.

The resulting spot weld dimensions are visualized in Figure 3, which shows the workpiece after the solidification has completed. The particles in red were melted during the heating process and solidified to form the spot weld, whereas the particles in blue stayed

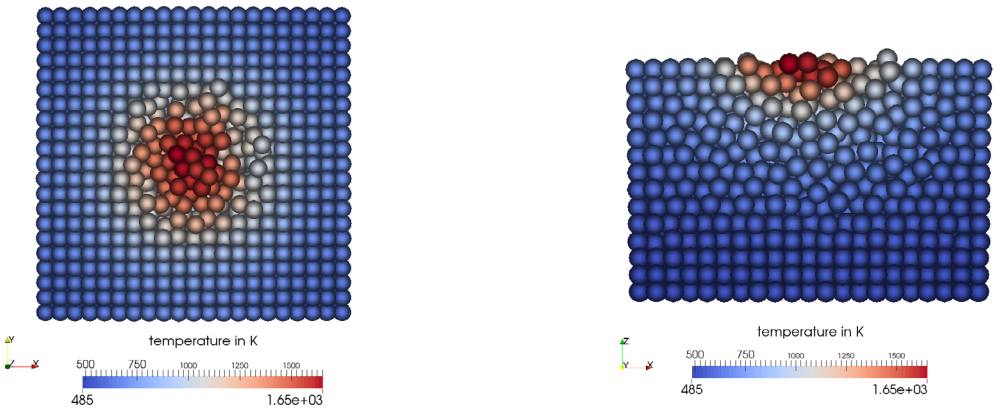

(a) Temperature distribution in the xy-plane (b) Temperature distribution in the xz-plane

Figure 1: Temperature distribution at t = 15 ms

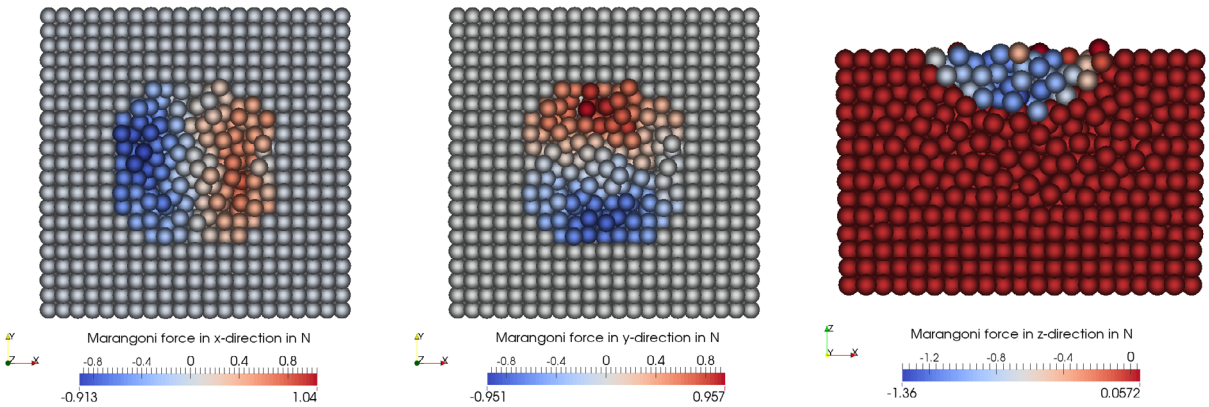

Figure 2: Marangoni force in x-, y-, and z-direction at t = 15 ms

solid during the welding process. The spot weld has a smaller depth than its radius, which is typical for conduction mode laser welding. The roughness of the surface after the weld solidified can be seen in the results.

3.2 Moving heat source

Next we investigate the process of seam welding where the laser beam is moved along a straight trajectory with a constant velocity of 1 m/min. At the beginning, the workpiece has the ambient temperature of 293 K. Through the moving laser beam, the material begins to melt and a weld pool with constant width and depth is formed. The shape of the weld pool and the position of the heat source after 50 ms can be seen in Figure 4(a). The effect of the surface tension force is noticeable at the border of the weld pool, since

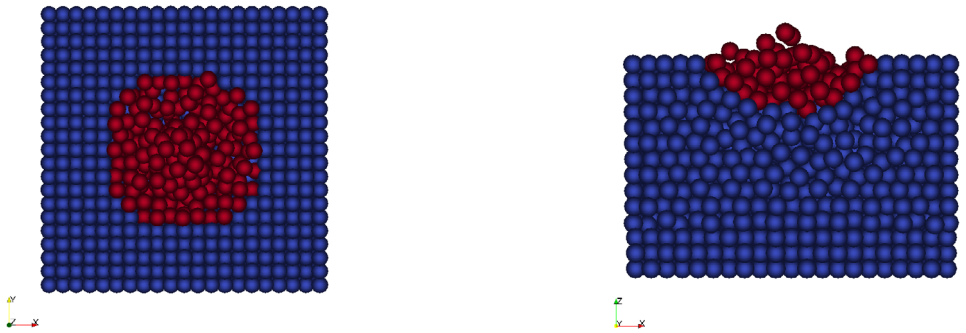

(a) Spot weld in the xy-plane (b) Spot weld in the xz-plane

Figure 3: Resulting spot weld colored in red

all particles are held together and the border particles do not move in the negative z-direction due to gravity. Figure 4(b) shows the corresponding temperature distribution in the xy-plane.

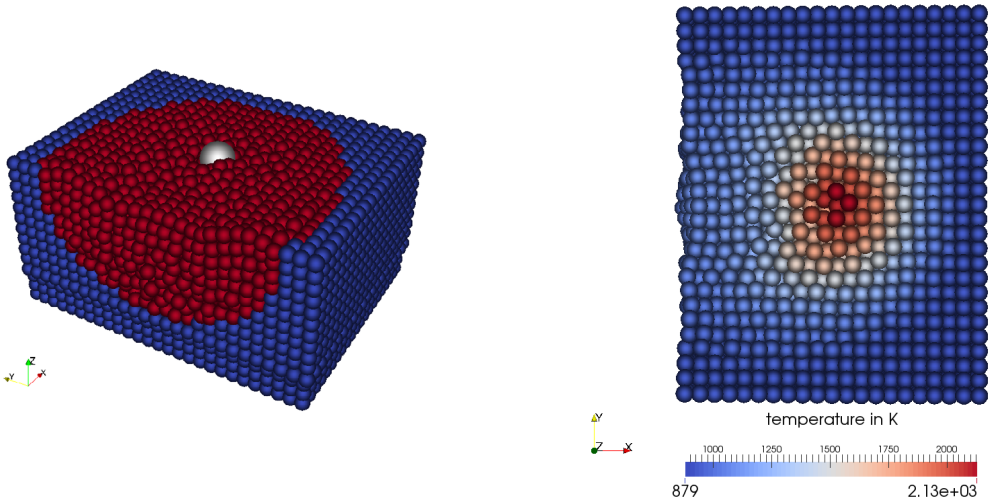

(a) Weld pool with heat source in grey (b) Temperature distribution in the xy-plane

Figure 4: Weld pool and temperature distribution at $t = 50$ ms

The Marangoni force at $t = 50$ ms in the case of a moving laser beam where the temperature gradient is constantly changing with time, is visualized in Figure 5. In the vicinity of the laser beam, the particles are accelerated in radial direction with the maximum force acting at the distance r_s. The value of the force in positive x-direction is slightly larger than in the negative direction, which is a consequence of the moving heat source. The force in z-direction has its minimum at the center of the heat source.

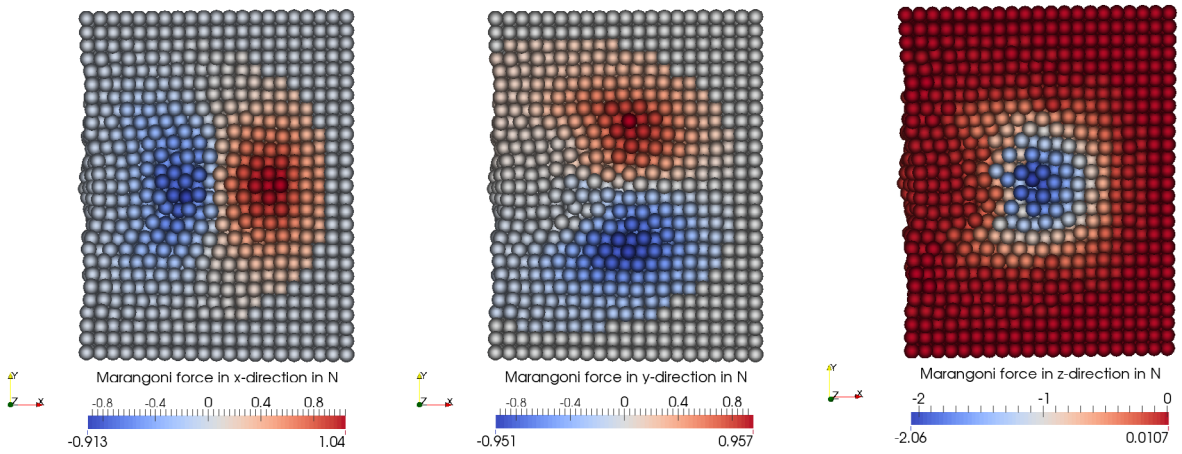

Figure 5: Marangoni force in x-, y-, and z-direction at $t = 50$ ms (view at xy-plane)

4 CONCLUSIONS

The process of conduction mode laser welding may be simulated with SPH and the obtained results are plausible. Compared to mesh-based methods, the advantage of using SPH lies in the relatively simple conversion from a solid to a fluid particle, the modeling of the free-surface melt flow, and the fluid-structure interaction. With welding simulations, the influence and sensitivity of each process parameter or material property on the weld pool dimensions and resulting weld can be investigated. Optimal process parameters like welding speed and laser power may be found for each welding application. The maximum temperature during the whole process can be monitored which might be useful for heat sensitive components that must not exceed a critical temperature value. For a quantitative validation, experiments under real operating conditions are planned to be carried out.

A multi-phase SPH formulation that is able to handle large density differences is in development. Then, the welding of different materials, e.g. steel and aluminum, could be simulated as well. Also, the modeling of laser deep penetration welding is in progress. For this physically much more complex welding technique, the liquid-vapor phase transition and the interaction of three different phases have to be modeled to achieve feasible results.

ACKNOWLEDGEMENT

The research leading to the presented results has received funding from the German Research Foundation (DFG) under the project EB 195/13-1 “Modeling of the capillary in laser beam penetration welding with the Smoothed Particle Hydrodynamics Method”. This support is highly appreciated. Helpful discussions with our project partners, especially Peter Berger of the Institut für Strahlwerkzeuge (IFSW), University of Stuttgart, are also gratefully acknowledged.

REFERENCES

[1] Batchelor, G.K.: An Introduction to Fluid Dynamics. Cambridge University Press, Cambridge (1974).

[2] Brackbill, J.U., Kothe, D.B., Zemach, C.: A Continuum Method for Modeling Surface Tension. Journal of Computational Physics **100**(2), 335–354 (1992).

[3] Cleary, P.W., Monaghan, J.J.: Conduction Modelling Using Smoothed Particle Hydrodynamics. Journal of Computational Physics **148**, 227–264 (1999).

[4] Courant, R., Friedrichs, K. and Lewy H.: On the Partial Difference Equations of Mathematical Physics. IBM Journal of Research and Development **11**(2), 215–234 (1967).

[5] Doghri, I.: Mechanics of Deformable Solids. Springer, Berlin (2000).

[6] Eringen, A.C.: Mechanics of Continua. Wiley, New York (1967).

[7] Fleißner, F.: Parallel Object Oriented Simulation with Lagrangian Particle Methods. Doctoral Thesis, Institute of Engineering and Computational Mechanics, University of Stuttgart. Shaker, Aachen (2010).

[8] Gingold, R.A., Monaghan, J.J.: Smoothed Particle Hydrodynamics: Theory and Application to Non-Spherical Stars. Monthly Notices of the Royal Astronomic Society **181**, 375–389 (1977).

[9] Hauke, G.: An Introduction to Fluid Mechanics and Transport Phenomena. Springer Netherlands, Dordrecht (2008).

[10] Hu, H., Argyropoulos, S.A.: Mathematical Modelling of Solidification and Melting: A Review. Modelling and Simulation in Materials Science and Engineering **4**, 371–396 (1996).

[11] Hügel, H., Graf, T.: Laser in der Fertigung – Grundlagen der Strahlquellen, Systeme, Fertigungsverfahren. Springer Vieweg, Wiesbaden (2014).

[12] Liu, G., Liu, M.: Smoothed Particle Hydrodynamics – A Meshfree Particle Method. World Scientific Publishing, Singapore (2003).

[13] Liu, M., Shao, J., Li, H.: Numerical Simulation of Hydro-Elastic Problems with Smoothed Particle Hydrodynamics Method. Journal of Hydrodynamics, Ser. B **25**(5), 673–682 (2013).

[14] Lobovský, L.; Groenenboom, P.H.L.: Smoothed Particle Hydrodynamics Modelling in Continuum Mechanics: Fluid-Structure Interaction. Applied and Computational Mechanics **3**(1), 101–110 (2009).

[15] Lucy, L.B.: A Numerical Approach to the Testing of the Fission Hypothesis. The Astronomical Journal **82**(12), 1013–1024 (1977).

[16] Monaghan, J.J.: Smoothed Particle Hydrodynamics. Annual Reviews in Astronomy and Astrophysics **30**, 543–574 (1992).

[17] Monaghan, J.J.: SPH without a Tensile Instability. Journal of Computational Physics **159**, 290–311 (2000).

[18] Monaghan, J.J.: Smoothed Particle Hydrodynamics. Reports on Progress in Physics **68**, 1703–1759 (2005).

[19] Monaghan, J.J., Gingold, R.A.: Shock Simulation by the Particle Method SPH. Journal of Computational Physics **52**, 374–389 (1983).

[20] Monaghan, J.J., Huppert, H., Worster, M.: Solidification Using Smoothed Particle Hydrodynamics. Journal of Computational Physics **205**, 684–705 (2005).

[21] Monaghan, J.J., Kos, A., Issa, N.: Fluid Motion Generated by Impact. Journal of Waterway **129**(6), 250–259 (2003).

[22] Morris, J.P., Fox, P.J., Zhu, Y.: Modeling Low Reynolds Number Incompressible Flows Using SPH. Journal of Computational Physics **136**, 214–226 (1997).

[23] Pasimodo: http://www.itm.uni-stuttgart.de/research/pasimodo/pasimodo_en.php. Accessed May 26, 2015.

[24] Steen, W.M., Mazumder, J.: Laser Material Processing. Springer, London (2010).

[25] Tong, M., Browne, D.J.: An Incompressible Multi-Phase Smoothed Particle Hydrodynamics (SPH) Method for Modelling Thermocapillary Flow. International Journal of Heat and Mass Transfer **73**, 284–292 (2014).